A Simulation Module for Microsystems using Hybrid Finite Elements: An Overview

Kunal D. Patil, Sreenath Balakrishnan, C. S. Jog and G. K. Ananthasuresh

Abstract We present here an overview of the work done in developing a simulation module for microsystems, which entails solving coupled partial differential equations concerning multiple physical phenomena. A distinguishing feature of this work is the use of hybrid finite elements wherein displacement and stress fields are independently interpolated to mitigate the ill effects of widely known locking phenomena in finite element analysis. A beneficial consequence of hybrid elements is that a single type of 3D element is suitable for structures of any proportions. Furthermore, for the same accuracy, the number of degrees of freedom needed in the hybrid finite element model is usually much lower as compared to the displacement-based model. In this chapter, after briefly discussing the essential aspects of hybrid elements, representative results in elastic deformation under mechanical loads, coupled electrostatic-elastic simulation, and coupled piezoresistive-elastic simulation are presented. Seamless interfacing of the analysis codes with pre- and post-processing modules of any finite element software is also noted.

Keywords Hybrid finite elements · Piezoresistitvity · Multi-physics simulations · Pull-in analysis

1 Introduction

Most physical phenomena encountered in microelectromechanical systems (MEMS) are governed by partial differential equations (PDEs) in the spatial domain and ordinary differential equations in the time domain. These PDEs are invariably coupled to one another because there is interdependence of one physical

K. D. Patil · S. Balakrishnan · C. S. Jog · G. K. Ananthasuresh (✉)
Computational Nanoengineering (CoNe) group and Mechanical Engineering,
Indian Institute of Science, Bangalore, India
e-mail: suresh@mecheng.iisc.ernet.in

K. J. Vinoy et al. (eds.), *Micro and Smart Devices and Systems*,
Springer Tracts in Mechanical Engineering, DOI: 10.1007/978-81-322-1913-2_21,

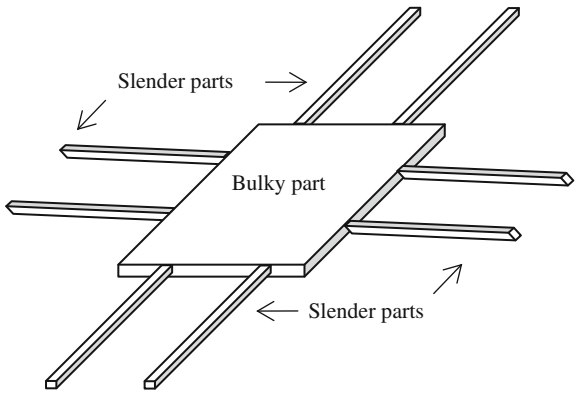

Fig. 1 A typical micromechanical structure with bulky and slender parts

energy domain to another (e.g., elastic to electrostatic and electrical to thermal) [1, 2]. Finite element analysis (FEA) is the most widely used numerical technique for solving the coupled equations in order to simulate the behavior of MEMS components and devices. However, even now in practice, there are two shortcomings to using FEA for the simulation of microsystems.

First, a large number of finite elements (i.e., a finely meshed model) is needed for good accuracy. The reason for this is twofold. First, microsystems components are often very thin in one dimension; and second, they contain relatively bulk bodies joined with slender components in the other two dimensions. Figure 1 illustrates a typical MEMS device where it can be seen that the out-of-plane thickness of the device is much smaller than the size in the in-plane direction. Therefore, a very fine mesh is needed to maintain the aspect ratio of the elements in the discretized mesh close to unity, as necessitated by the traditional finite elements. Also noticeable in Fig. 1 are very narrow portions, namely beams, connected to a wide plate. Bulky portions, which do not undergo much elastic deformation, need not be meshed as finely as the slender portions, but there should be smooth transitions in the mesh. This means that if the same type of finite element is used for slender and bulky portions, one should be careful in changing the density and size of elements while meshing the model. An alternative is to use different types of elements (e.g., beam, plate, and shell) for different portions. The mathematical implication of the type of element is the degree of the underlying interpolating function called the *shape function*. Incompatibility in the interpolating shape functions and the aspect ratios of elements leads to inaccurate results due to what are known as *shear* or *membrane locking phenomena* [3]. Deciding on the suitability of an element type for a given problem demands considerable expertise from the users. Given the multidisciplinary nature of the microsystems technology, it is not fair to expect all users to be aware of the intricacies of solving PDEs using FEA. Thus, one type of elements for any structure, however complex its geometry may be, is preferable. At the same time, too fine a mesh with one element type is an overkill because it leads to excessive computation time.

The second shortcoming of FEA arises while solving coupled PDEs; the method adopted by most simulation algorithms and commercial microsystem simulation software is a staggered approach. That is, if there are two coupled fields, the algorithm solves for one field and then takes the coupling variables to solve for the other field and iterates between the two fields in a sequential manner. As opposed to this, in a combined approach, all the PDEs related to multiple phenomena are solved simultaneously. This improves the computational efficiency.

Based on the foregoing, the aim of this chapter is to describe a simulation strategy for microsystem components and devices using a single type of hybrid finite element and an integrated strategy for solving coupled PDEs. While this approach applies to a number of problems within the MEMS field, only deformation and stress analysis under purely mechanical loads, coupled elastic-electrostatic analysis, and coupled elastic-piezoresistive analysis are explained in detail. Modal analysis, coupled electro-thermal-elastic analysis, etc., can also be solved using similar methods.

The rest of the chapter is organized as follows. Section 2 describes the theory of the hybrid finite elements. Section 3 exemplifies the efficacy of the hybrid FEA for micromechanical structures under purely mechanical loads. Sections 4 and 5 contain discussions of coupled elastic-electrostatic and elastic-piezoresistive simulations, respectively. Integration issues are briefly noted in Sect. 6. Section 7 has concluding remarks.

2 Hybrid Finite Element Procedure

Hybrid finite elements [4–8] are known to give high accuracy with only a few elements. They are not prone to become artificially stiff when the elements are thin in one direction or distorted otherwise. They are also largely free from locking phenomena. In [7], a 27-noded hybrid finite element formulation was proposed. It enables cost-effective FEA for structures that have narrow and thin parts in conjunction with bulky and wide parts. This is a common occurrence in microsystems as shown in Fig. 1. We adopt the hybrid elements for microsystem simulation as reported in [9]. A brief theory of hybrid finite element procedure is therefore pertinent here and is presented next for the linear problem by first discussing the usual displacement-based FEA. Readers interested in the nonlinear formulation of the hybrid elements may consult Ref. [10].

The PDE that governs the elastic deformation of a structural element occupying a domain Ω with the boundary $\partial\Omega$ and subjected to body forces $\mathbf{f}_b$ (e.g., gravity or inertia forces) and boundary force $\mathbf{f}_t$ (e.g., fluid pressure or electrostatic force), is as follows:

$$\begin{aligned}
&\nabla \cdot \boldsymbol{\tau} + \mathbf{f}_b = 0 \\
&\boldsymbol{\tau} = \mathbf{D}_m : \boldsymbol{\varepsilon} \\
&\boldsymbol{\varepsilon} = \left\{ \nabla \mathbf{u} + (\nabla \mathbf{u})^T \right\} / 2 \\
&\mathbf{f}_t = \boldsymbol{\tau}\, \hat{\mathbf{n}} \text{ on } \partial\Omega_t \\
&\mathbf{u} = \mathbf{u}^* \text{ on } \partial\Omega_u
\end{aligned} \tag{1}$$

where $\boldsymbol{\tau}$ is the stress, $\boldsymbol{\varepsilon}$ the strain, $\mathbf{D}_m$ the constitutive matrix relating $\boldsymbol{\tau}$ and $\boldsymbol{\varepsilon}$, and $\mathbf{u}$ the displacement vector. The force applied on the boundary $\partial\Omega_t$ is $\mathbf{f}_t$; the specified displacement on the boundary $\partial\Omega_u$ is $\mathbf{u}^*$, and $\partial\Omega = \partial\Omega_t \cup \partial\Omega_u$. The variational form of the PDE in Eq. (1) is

$$\int_{\Omega} \boldsymbol{\varepsilon}(\delta\mathbf{u}) : \mathbf{D}_m : \varepsilon(\mathbf{u})\, d\Omega - \int_{\partial\Omega_t} \delta\mathbf{u} \cdot \mathbf{f}_t\, d(\partial\Omega) - \int_{\Omega} \delta\mathbf{u} \cdot \mathbf{f}_b\, d\Omega = 0 \;\forall \delta\mathbf{u} \tag{2}$$

where $\delta\mathbf{u}$ is the variation of $\mathbf{u}$. In displacement-based FEA, $\mathbf{u}$ and $\delta\mathbf{u}$ are interpolated within the element using shape functions $\mathbf{N}$ and the nodal displacement degree-of-freedom vector $\mathbf{u}_e$ of an element:

$$\mathbf{u} = \mathbf{N}\mathbf{u}_e \;\text{ and }\; \delta\mathbf{u} = \mathbf{N}\delta\mathbf{u}_e \tag{3}$$

We differentiate the displacement as per the definition of the strain given in the third line of Eq. (1) to get the strain displacement relationship for an element:

$$\boldsymbol{\varepsilon}_e = \mathbf{B}\mathbf{u}_e \tag{4}$$

By substituting from Eqs. (3) and (4) into Eq. (2), performing integration over all discretized elements, and assembling the global stiffness matrix $\mathbf{K}$, we get

$$\mathbf{K}\mathbf{U} = \mathbf{f} \tag{5}$$

where

$$\begin{aligned}
\mathbf{K} &= \sum_{\text{All elements}} \int_{\Omega_e} \mathbf{B}^{\mathbf{T}} \mathbf{D}_m \mathbf{B}\, \mathrm{d}\Omega_e \\
\mathbf{f} &= \sum_{\text{All elements}} \left(\int_{\partial\Omega_{et}} \mathbf{N}^T \mathbf{f}_t\, \mathrm{d}(\partial\Omega) + \int_{\Omega_e} \mathbf{N}^T \mathbf{f}_b\, \mathrm{d}\Omega \right)
\end{aligned} \tag{6}$$

where $\mathbf{U}$ and $\mathbf{f}$ are the global displacement and force vectors.

Thus, the usual finite element analysis described in the preceding equations, assumes only displacement as an independent variable in order to interpolate within the element using the values at the nodes. Strains and stresses are then

computed using the strain-displacement and constitutive (i.e., stress-strain) relationships, respectively. On the other hand, in the hybrid finite element, both displacement and stresses are independently interpolated. Consequently, an additional condition is necessary to ensure compatibility between independently interpolated displacements and stresses. Thus, in addition to Eq. (2), we have

$$\int_{\Omega} \delta\boldsymbol{\tau} : \left\{\boldsymbol{\varepsilon}(\mathbf{u}) - \mathbf{D}_m^{-1} : \boldsymbol{\tau}\right\} \mathrm{d}\Omega = 0 \;\; \forall \delta\boldsymbol{\tau} \tag{7}$$

where $\delta\boldsymbol{\tau}$ is the variation of the stress field $\boldsymbol{\tau}$. The two stress fields are interpolated as follows.

$$\boldsymbol{\tau} = \mathbf{P}\tau_e \text{ and } \delta\boldsymbol{\tau} = \mathbf{P}\delta\boldsymbol{\tau}_e \tag{8}$$

where $\boldsymbol{\tau}_e$ and $\delta\boldsymbol{\tau}_e$ denote nodal stresses of an element and their variations, respectively. Choosing the interpolating shape functions $\mathbf{P}$ in Eq. (8) is crucial here because it is to be done to avoid the so-called locking phenomena [7].

Now, Eq. (2) [after $\mathbf{D}_m$: $\boldsymbol{\varepsilon}(\mathbf{u})$ is replaced with $\boldsymbol{\tau}$)] and Eq. (7) leads to the following system of equations for the discretized model, with T denoting the global stress vector:

$$\begin{bmatrix} \mathbf{0} & \mathbf{G}^T \\ \mathbf{G} & -\mathbf{H} \end{bmatrix} \begin{Bmatrix} \mathbf{U} \\ \mathrm{T} \end{Bmatrix} = \begin{Bmatrix} \mathbf{f} \\ \mathbf{0} \end{Bmatrix} \tag{9}$$

where

$$\mathbf{G} = \int_{\Omega} \mathbf{P}^T \mathbf{B} \, \mathrm{d}\Omega \tag{10a}$$

$$\mathbf{H} = \int_{\Omega} \mathbf{P}^T \mathbf{D}_m^{-1} \mathbf{P} \, \mathrm{d}\Omega \tag{10b}$$

At this point, another important simplification is made to eliminate the stress degrees of freedom of all the elements (i.e., $\mathbf{T}$) by using the second equation of Eq. (9).

$$\mathbf{T} = \mathbf{H}^{-1}\mathbf{G}\mathbf{U} \tag{11}$$

Thus, we are left with

$$\mathbf{K}_h\mathbf{U} = \mathbf{f} \tag{12}$$

where

$$\mathbf{K}_h = \mathbf{G}^T \mathbf{H}^{-1} \mathbf{G} \tag{13}$$

is the stiffness matrix of the hybrid element. Now, even though the stress field was interpolated, its degrees of freedom are "condensed out" by eliminating them in terms of the usual displacement degrees of freedom. So, apart from the additional computation involved in assembling and inverting $\mathbf{K}_h$, the procedure is the same as the usual finite element method. Thus, there is no difference from the user's viewpoint because only the stiffness matrix has changed from $\mathbf{K}$ in Eq. (6) to $\mathbf{K}_h$ in Eq. (13).

Choosing appropriate number of nodes for a 3D element and suitable shape functions $\mathbf{P}$ for them [see Eq. (8)] is the key to the hybrid FEA method. The larger the number of nodes in an element is, the larger will be the element-level computation. But much fewer elements are needed to mesh a structure. That is, it should be noted that a 27-noded hexahedral hybrid brick element needs much fewer elements (i.e., a coarse mesh) for a given structure to give an accurate solution as compared to an eight-noded brick element. So, there is a trade-off between the extent of coarseness of an FE mesh and the number of nodes in an element. Based on numerical experimentation, we had reported in [9] the relative order of accuracy by implementing different elements. The elements in decreasing accuracy are: 27-noded hybrid element, 8-noded hybrid brick element, 27-noded displacement brick element, 18-noded displacement brick element, 10- and 11-noded tetrahedral displacement wedge elements, and 6-noded pentahedral hybrid wedge element.

Even though the 27-noded hybrid element gives the most accuracy, it has two limitations: (i) the meshing algorithm for 27-noded 3D elements is not common in FEA software programs, and (ii) 27-noded element entails the inversion of a 90×90 element-level matrix as can be understood from Eq. (13). So, in spite of the fact that the 27-noded element suffices to have a coarse mesh, it is not the best element in practice. In view of the computation time, accuracy, and meshing capability of the chosen software for integration (NISA from Cranes Software International Limited, here), we have implemented 8-noded hybrid hexahedral and 6-noded pentahedral hybrid wedge element in this work. These elements are shown in Fig. 2.

3 Elastic Simulation of Micromechanical Structures

In this section, we illustrate how hybrid and commonly used displacement finite elements perform relative to each other in terms of accuracy and computational efficiency. Toward this, we compare the results of our hybrid finite element code with the displacement element-based FEA in commercial software. It must be noted at the outset that this is not a comparison of our code with the commercial software because we are not comparing with the best elements of commercial

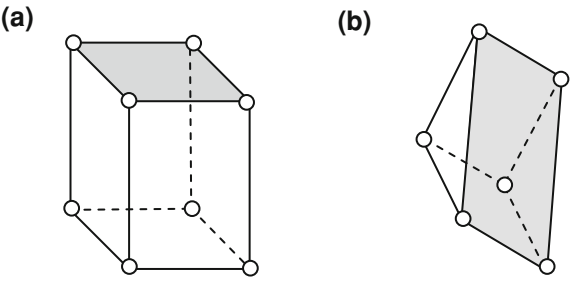

Fig. 2 **a** Eight-noded hexahedral brick element for the interior and **b** six-noded pentahedral hybrid wedge element for the boundary

software for the chosen problems. It is a known fact that commercial software adopt a variety of techniques to avoid locking phenomena. Reduced integration, hour-glass control, etc., are some of the methods [3]. But a priori knowledge of which element to use for which problem cannot be presumed. An element type that works for one problem might not work for another. This is an advantage in favor of the hybrid elements. In summary, we reiterate that in what follows we simply compare the performance of hybrid elements in our implementation with that of the displacement element-based implementations, without any ad hoc modifications, in commercial software. Here, we use ABAQUS (www.simulia.com) and NISA (www.nisasoftware.com). But similar comparisons will come true with any other software. Minor discrepancies will be there because one can never be sure of small differences in implementation.

In all examples in this chapter, we use eight-noded hexahedral elements for the interior and six-noded pentahedral wedge elements, the latter meeting the demands of corners and edges, in the hybrid finite element code in our implementation. We use the same meshed models, but with displacement-based elements in NISA and ABAQUS. NISA uses full integration, whereas ABAQUS uses selective integration in its C3D8 (brick) and C3D6 (wedge) elements.

The following points are to be noted in interpreting the results presented next. First, in tables and figures, we show the accuracy parameter of a result as a % value where the reference value is either calculated using an analytical solution (when it is available) or computed using the hybrid code with sufficiently fine mesh. Second, sometimes, the hybrid code could not be run for very fine meshes because of the limitation of the memory of the computer. But it does not matter because the hybrid code gives accurate results with just a few degrees of freedom in the meshed model. Third, computing time is also indicated for the runs on the same desktop computer for all three implementations (hybrid code, NISA, and ABAQUS).

3.1 Example 1: Folded-Beam Suspension

The geometry of the folded-beam suspension, which is a compliant substitute for a sliding joint, is shown in Fig. 3. It consists of two bulky portions connected with four slender beams in the left symmetric half. The right most edge is constrained to move

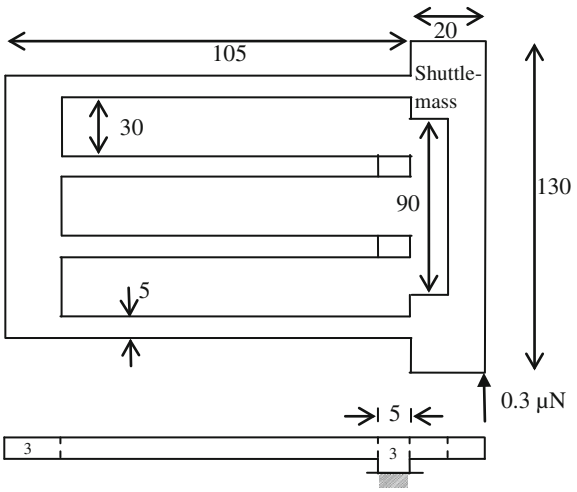

Fig. 3 Symmetric half-model of the folder-beam suspension (all dimensions are in μm)

along the edge, but not perpendicular to it in this symmetric half-model. An analytical solution is available [11] for the displacement of this model for a force applied on the bulky portion, called the *shuttle-mass*, at the bottom, as can be seen in Fig. 3.

Three different meshes were considered with 1056, 10,806, and 3,01,830 degrees of freedom (DoF). The results are shown in Table 1. The table shows the displacement of the shuttle-mass, the accuracy of this displacement relative to the known analytical solution, and the computation time. Figure 4 shows accuracy vs. DoF using results obtained by running many meshed models. In Table 1 and Fig. 4, it can be seen that the hybrid code achieves high accuracy with very few degrees of freedom. Therefore, its computation time is also much less as compared to those of the displacement elements in ABAQUS and NISA.

Similar trends were seen with other examples considered. They included a pressure-sensor diaphragm, a micromachined gripper, a gyroscope's suspension, etc. The latter two consisted of curved geometries and the last, the suspension of a ring-gyroscope, had only slender segments. The efficacy of hybrid elements was seen in all examples considered for a comparative study. The details are in [9].

The algorithm for the purely elastic analysis included geometric nonlinearity. It also has the capability to do dynamic analysis, which is not described here. We consider coupled analyses next. When we do coupled analysis, we use hybrid elements only for the elastic analysis, but not for the others. The reason for this is that the governing PDEs of the others are not known to exhibit locking phenomena.

4 Coupled Electrostatic-Elastic Simulation

Coupled electrostatic-elastic simulation is most common in microsystem simulation because electrostatic actuation is the most widely used actuation technique in microsystems. Here, we have developed algorithms for purely electrostatic

Table 1 Comparison of displacement, accuracy relative to the analytical result, and computing time for the folded-beam suspension

DoF	Hybrid	ABAQUS	NISA
1,056	0.12 μm	0.03 μm	0.02 μm
	97.5 %	20.7 %	17.8 %
	0.23 s	0.10 s	0.08 s
10,806	0.12 μm	0.09 μm	0.09 μm
	99.9 %	74.6 %	72.9 %
	1.84 s	0.80 s	0.93 s
3,01,830	Not run.	0.12 μm	0.12 μm
		99.9 %	99.9 %
		25.1 s	281.8

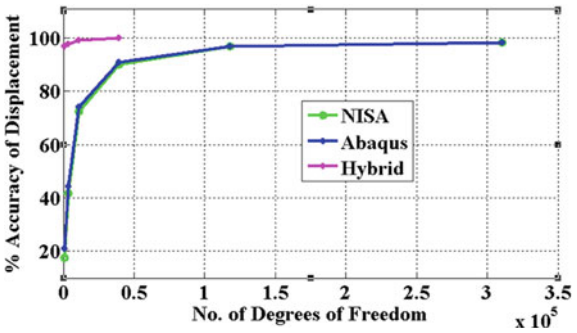

Fig. 4 Comparison of accuracy of the displacement for the example of the folder-beam suspension

simulation (i.e., capacitance calculation) and coupled electrostatic-elastic simulation. The latter is developed for geometrically nonlinear elastic behavior in static and dynamic conditions. It may be noted that only elastic analysis uses hybrid elements. Electrostatic analysis does not require hybrid elements, as we do not see the problems akin to locking here. One novel feature of the algorithm is that it is an *integrated* (some call it *monolithic* [11, 12]) procedure in that the displacement and electrical potential are solved together by combining their respective governing equations. This is in contrast to the staggered approach where the solver routines for the two are called alternately in an iterative procedure [13]. The direct coupling approach followed in the work presented in this chapter makes it computationally more efficient than the existing approaches. This approach is also useful in optimization of MEMS structures [14]. The theory of the integrated formulation is presented next.

4.1 Coupled Electrostatic-Elastic Formulation

The governing equations of the coupled electrostatic-elastodynamic problem can be written together as follows.

$$\begin{aligned}
&\nabla \cdot (\mathbf{F}\tau) + \rho_0 \mathbf{b}^{\mathbf{0}} = \rho_0 \frac{\partial^2 \mathbf{u}}{\partial t^2} \text{ on } \Omega \\
&\boldsymbol{\tau} = \boldsymbol{\tau}_{\text{mech}} + \boldsymbol{\tau}_{\text{elec}} \\
&\mathbf{t}^0 = \bar{\mathbf{t}}^0 \text{ on } \partial\Omega_t \\
&\mathbf{u} = \mathbf{0} \text{ on } \partial\Omega_u \\
&\nabla \cdot \mathbf{D}_e = 0 \\
&\mathbf{D}_e = \sigma_e J \mathbf{C}^{-1} \mathbf{E} + \mathbf{d}\varepsilon_L \\
&\mathbf{E} = -\nabla_X \phi
\end{aligned} \tag{14}$$

where $\mathbf{F}$ is the deformation gradient, $\boldsymbol{\tau}$ the total stress that includes elastic (i.e., mechanical stress) component $\boldsymbol{\tau}_{\text{mech}}$ and electrostatic (the so-called Maxwell stress) component $\boldsymbol{\tau}_{\text{elec}}$, ρ^0 the mass density, $\mathbf{b}^0$ the body force, $\mathbf{u}$ the displacement vector, Ω the domain over which the problem is posed, $\mathbf{t}^0$ the surface force and $\bar{\mathbf{t}}^0$ its specified value on a portion of the boundary $\partial\Omega_t$, $\partial\Omega_u$ the boundary on which displacement is specified (i.e., anchored portion), $\mathbf{D}_e$ the electric displacement vector, σ_e the electrical conductivity, J the determinant of $\mathbf{F}$, $\mathbf{C}$ the right Cauchy-Green strain tensor, $\mathbf{d}$ the third-order piezoelectric tensor, $\boldsymbol{\varepsilon}_L$ the Lagrangian strain, ϕ the electric potential, and $\mathbf{E}$ the electric field. The expression for the Maxwell stress $\boldsymbol{\tau}_{\text{elec}}$ and the constitutive relationship for the elastic behavior are not given here. Interested readers may refer to Ref. [15]. The permittivity is also missing here, but it is taken implicitly as electrical conductivity as far as the numerical values go. There is some inherent ambiguity in this issue [12], which we take care of in the implementation.

In the usual displacement formulation, the weak form of the governing equations are:

$$\begin{aligned}
&\int_\Omega \boldsymbol{\tau} : \delta\boldsymbol{\varepsilon}_L \, \mathrm{d}\Omega = \int_\Omega \rho_0 \delta\mathbf{u} \cdot \mathbf{b}^0 \, \mathrm{d}\Omega + \int_{\partial\Omega_t} \delta\mathbf{u} \cdot \bar{\mathbf{t}}^0 \, \mathrm{d}\partial\Omega_t \\
&\int_\Omega \nabla\delta\phi \cdot \left(\sigma_e J \mathbf{C}^{-1} \nabla\phi + \mathbf{d}\varepsilon_L\right) \mathrm{d}\Omega = -\int_{\partial\Omega_d} \delta\phi \, D_{\text{en}} \, \mathrm{d}\partial\Omega
\end{aligned} \tag{15}$$

where D_{en} is the normal component of $\mathbf{D}_e$ and the symbol δ indicates the variation or the weak variable. In the hybrid formulation, one more equation is added by making stress also an independent variable.

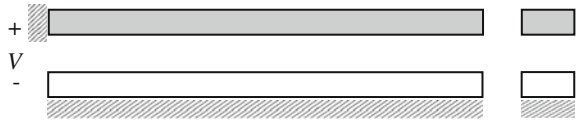

Fig. 5 A cantilever beam considered for the electrostatic pull-in analysis: lateral and side views

$$\int_{\Omega} \delta\boldsymbol{\tau}_{\text{mech}} : \left[\boldsymbol{\varepsilon}_L(\mathbf{u}) - \mathbf{D}_m^{-1} : \boldsymbol{\tau}_{\text{mech}}\right] d\Omega = 0 \;\forall\, \delta\boldsymbol{\tau}_{\text{mech}} \tag{16}$$

By using interpolation functions, which is the key to the hybrid element formulation, the discretized equations for incremental updating of displacements and electric potential are given by

$$\begin{aligned} \mathbf{K}_{uu}\Delta\tilde{\mathbf{u}} + \mathbf{K}_{u\phi}\Delta\tilde{\phi} &= \Delta\mathbf{f}_u \\ \mathbf{K}_{\phi u}\Delta\tilde{\mathbf{u}} + \mathbf{K}_{\phi\phi}\Delta\tilde{\phi} &= \Delta\mathbf{f}_\phi \end{aligned} \tag{18}$$

The cross-coupling terms involving $\mathbf{K}_{u\phi}$ and $\mathbf{K}_{\phi u}$ in Eq. (18) occur in only fully coupled integrated (i.e., "monolithic") formulation and not in the staggered formulation. It may be noticed that the stress terms are condensed out in this coupled simulation as they would be in the purely elastic formulation.

Shown in Fig. 5 are the geometric details of a sample problem pertaining to electrostatically actuated cantilever beam with an electrode underneath. The simulation result is shown in Fig. 6. It can be seen in Fig. 6 that the electrostatic pull-in result obtained using our integrated hybrid code compares well with that of the commercial code using COMSOL MultiPhysics (www.comsol.com). This confirms the accuracy of the code developed. More details of this problem and other examples can be found in [15].

5 Coupled Elastic-Piezoresistive Simulation

Piezoresistors are often used in MEMS devices. Modeling of the piezoresistive effect entails solving the electrical conduction equation because only conducting materials show piezoresistive effect, i.e., their electrical resistivity changes by measurable extent in response to mechanical stress. Thus, we begin with

$$\nabla \cdot \mathbf{J}_e = 0 \tag{19}$$

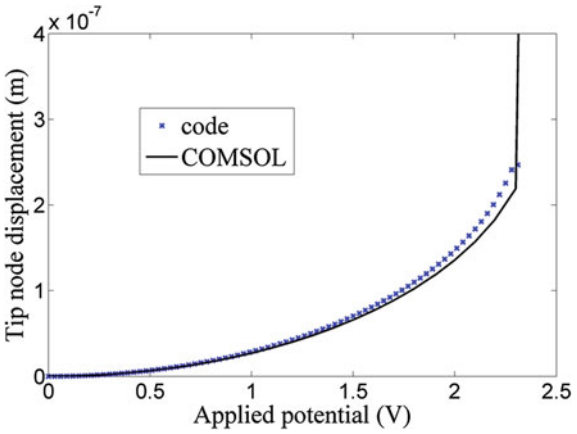

Fig. 6 The displacement of the electrostatically actuated cantilever beam against applied DC voltage until pull-in: comparison of the results of the integrated hybrid code and staggered COMSOL code

where $\mathbf{J}_e$ is the current density vector. The current density vector, at the microscopic level, is related to the electric field by Ohm's law:

$$\mathbf{J}_e = \boldsymbol{\sigma}_e \mathbf{E} \tag{20}$$

where $\boldsymbol{\sigma}_e$ is the conductivity matrix and $\mathbf{E}$ the electric field, which is given by the gradient of the electric potential, ϕ.

$$\mathbf{E} = \nabla \phi \tag{21}$$

The conductivity is the reciprocal of electrical resistivity: $\boldsymbol{\sigma}_e = \boldsymbol{\rho}^{-1}$. The resistivity of piezoresistive materials is modeled, up to first order, in terms of stress, $\boldsymbol{\tau}$.

$$\boldsymbol{\rho}_e = \boldsymbol{\rho}_e^0 \{\mathbf{I} + \pi : \tau\} \tag{22}$$

where $\boldsymbol{\rho}_e^0$ is the resistivity in the unstressed state, $\boldsymbol{\pi}$ the fourth-order piezoresistivity tensor and $\boldsymbol{\tau}$ the second-order stress tensor. This requires us to have both the piezoresistive and stress tensors expressed in the same coordinate system.

The values of the piezoresistive coefficients in the piezoresistive tensor are commonly given in a coordinate system that aligns with the <100> crystallographic directions. On the other hand, the design of a micromechanical component may be such that it is inconvenient to calculate the stress tensor in that coordinate system. For instance, if a piezoresistor is embedded in a cantilever, the piezoresistive tensor is given along the local coordinate system aligned with crystallographic directions, while it is convenient to calculate the stress tensor in the cantilever's coordinate system aligned with its longitudinal axis. The transformation of the stress to the crystallographic coordinate system is tedious because the transformation has to be carried out at every point in the domain where the change in resistivity needs to be calculated. It may be recalled that the

piezoresistivity tensor is a property of the material. Thus, once transformed from the crystallographic direction to the cantilever's coordinate system, it will remain the same at every point in the domain.

Here, we observe that the transformed piezoresistive tensor can have more than three independent coefficients contrary to only three that a cubic material has along a coordinate system aligned with the <100> crystal axes. We argue here that approximation of the transformed piezoresistive tensor to one with only three independent coefficients can sometimes lead to considerable errors in the calculated piezoresistive effect. This is a noteworthy point because some of the software packages that simulate the piezoresistive effect (e.g., CoventorWare; www.coventor.com) do not have convenient interfaces for the calculation of the complete piezoresistivity tensor when the crystal lattice is arbitrarily oriented with respect to the principal directions of the micromechanical component. In what follows, we discuss how the fourth-order piezoresistive tensor can be transformed from one Cartesian coordinate system to another. The numerical details of the next two sections can be found in [16].

5.1 Coordinate Transformation of the Piezoresistive Tensor

The piezoresistivity tensor $\boldsymbol{\pi}$ in Eq. (22) has both minor and major symmetries. Consequently, it requires only 36 independent components (instead of 81 in the case of a general fourth-order tensor). It can therefore be written as a 6×6 matrix [2]. For cubic materials, there are additional symmetries when the piezoresistivity tensor is aligned with the <100> lattice directions. Then, as stated earlier, the piezoresistivity tensor contains only three independent coefficients [2]. They are as follows:

$$\boldsymbol{\pi}_{\langle 100\rangle} = \begin{bmatrix} \pi_{11} & \pi_{12} & \pi_{12} & 0 & 0 & 0 \\ \pi_{12} & \pi_{11} & \pi_{12} & 0 & 0 & 0 \\ \pi_{12} & \pi_{12} & \pi_{11} & 0 & 0 & 0 \\ 0 & 0 & 0 & \pi_{44} & 0 & 0 \\ 0 & 0 & 0 & 0 & \pi_{44} & 0 \\ 0 & 0 & 0 & 0 & 0 & \pi_{44} \end{bmatrix} \tag{23}$$

where the indices are compressed according to the usual convention, $11 \rightarrow 1$, $22 \rightarrow 2$, $33 \rightarrow 3$, $12 \rightarrow 4$, $23 \rightarrow 5$, $31 \rightarrow 6$. This means that the (1, 2, 2, 3) position of the fourth-order tensor is the coefficient at the (4, 5) position in the matrix notation. Next, consider the transformation of second-order tensors between two Cartesian coordinate systems [17]:

$$\mathbf{T}' = \mathbf{RTR}^{-1} \tag{24}$$

where $\mathbf{R}$ is the rotation matrix between the two coordinate systems given by

$$\mathbf{R} = \begin{bmatrix} l_1 & l_2 & l_3 \\ m_1 & m_2 & m_3 \\ n_1 & n_2 & n_3 \end{bmatrix} \tag{25}$$

and the directions of the coordinate axes of the rotated coordinate system expressed in terms of the original coordinate system is

$$\mathbf{x}' = \begin{bmatrix} l_1 \\ m_1 \\ n_1 \end{bmatrix}, \mathbf{y}' = \begin{bmatrix} l_2 \\ m_2 \\ n_2 \end{bmatrix}, \mathbf{z}' = \begin{bmatrix} l_3 \\ m_3 \\ n_3 \end{bmatrix} \tag{26}$$

Since a symmetric second-order tensor can be represented as a 6-element column vector using the convention for compression of indices, we can write

$$\mathbf{T}^T = [\,\mathbf{T}_1 \quad \mathbf{T}_2 \quad \mathbf{T}_3 \quad \mathbf{T}_4 \quad \mathbf{T}_5 \quad \mathbf{T}_6\,] \tag{27}$$

By using the vector representation of the symmetric second-order tensor shown in the preceding equation, the coordinate transformation can be carried out using a single 6×6 rotation matrix multiplication

$$\mathbf{T}' = \mathbf{R}_{6\times6}\mathbf{T} \tag{28}$$

where $\mathbf{R}_{6\times6}$ is given by

$$\begin{bmatrix} l_1^2 & m_1^2 & n_1^2 & 2l_1m_1 & 2m_1n_1 & 2n_1l_1 \\ l_2^2 & m_2^2 & n_2^2 & 2l_2m_2 & 2m_2n_2 & 2n_2l_2 \\ l_3^2 & m_3^2 & n_3^2 & 2l_3m_3 & 2m_3n_3 & 2n_3l_3 \\ l_1l_2 & m_1m_2 & n_1n_2 & l_1m_2 + l_2m_1 & m_1n_2 + m_2n_1 & n_1l_2 + n_2l_1 \\ l_2l_3 & m_2m_3 & n_2n_3 & l_2m_3 + l_3m_2 & m_2n_3 + m_3n_2 & n_2l_3 + n_3l_2 \\ l_3l_1 & m_3m_1 & n_3n_1 & l_3m_1 + l_1m_3 & m_3n_1 + m_1n_3 & n_1l_3 + n_1l_3 \end{bmatrix} \tag{29}$$

Similar to the case of second-order tensors, the coordinate transformation of fourth-order tensors is given by [17]

$$\boldsymbol{\pi}' = \mathbf{R}_{6\times6}\pi\mathbf{R}_{6\times6}^{-1} \tag{30}$$

When the transformed coordinate system differs from the original coordinate system only through a rotation about the z-axis, the transformed piezoresistive tensor expression reduces to a 6×6 matrix:

$$\boldsymbol{\pi}' = \begin{bmatrix} \frac{3\pi_{11}+\pi_{12}+\pi_{44}+(\pi_{11}-\pi_{12}-\pi_{44})\cos(4\theta)}{4} \\ \frac{\pi_{11}+3\pi_{12}-\pi_{44}-(\pi_{11}-\pi_{12}-\pi_{44})\cos(4\theta)}{4} \\ \pi_{12} \\ \frac{(-\pi_{11}+\pi_{12}+\pi_{44})\sin(4\theta)}{4} \\ 0 \\ 0 \end{bmatrix} \begin{bmatrix} \frac{\pi_{11}+3\pi_{12}-\pi_{44}-(\pi_{11}-\pi_{12}-\pi_{44})\cos(4\theta)}{4} \\ \frac{3\pi_{11}+\pi_{12}+\pi_{44}+(\pi_{11}-\pi_{12}-\pi_{44})\cos(4\theta)}{4} \\ \pi_{12} \\ -\frac{(-\pi_{11}+\pi_{12}+\pi_{44})\sin(4\theta)}{4} \\ 0 \\ 0 \end{bmatrix} \begin{bmatrix} \pi_{12} & \frac{(-\pi_{11}+\pi_{12}+\pi_{44})\sin(4\theta)}{2} & 0 & 0 \\ \pi_{12} & -\frac{(-\pi_{11}+\pi_{12}+\pi_{44})\sin(4\theta)}{2} & 0 & 0 \\ \pi_{11} & 0 & 0 & 0 \\ 0 & (\pi_{11}-\pi_{12}-\pi_{44})\sin^2(2\theta)+\pi_{44} & 0 & 0 \\ 0 & 0 & \pi_{44} & 0 \\ 0 & 0 & 0 & \pi_{44} \end{bmatrix} \tag{31}$$

where θ is the angle of rotation about the z-axis of the transformed coordinate system with respect to the original coordinate system.

5.2 An example

We now consider an example of a representative micromechanical structure where taking only three-independent-parameter piezoresistive tensor given in Eq. (23) leads to substantial error as opposed to taking the full transformed tensor given in Eq. (31). This happens, as noted earlier, when the crystallographic directions are not aligned with the longitudinal axis of the deforming slender element. Toward this, consider a micro-mirror that twists about a single axis as shown in Fig. 7. It has a wide plate in the middle with twisting beams on either side. When there is a force on the vertical faces that are oriented along the longitudinal axis of the structure, in the opposing directions so as to cause the tilting of the plate about the

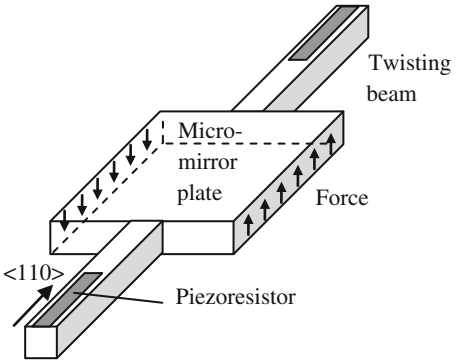

Fig. 7 A example micro-mirror structure in which the piezoreistor's <110> axis is aligned with the longitudinal axis of the twisting beams

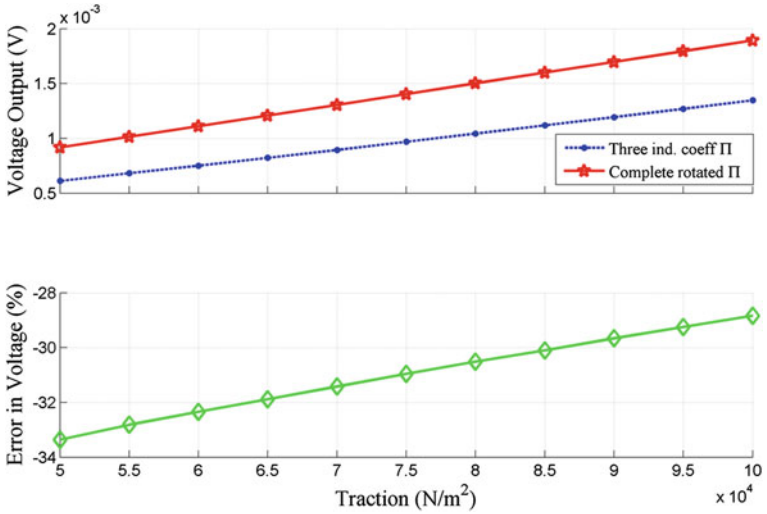

Fig. 8 The discrepancy in the computed voltage of the Wheatstone bridge circuit when the transformed piezoresistor has all parameters and only three parameters

longitudinal axis, the beams must twist. Assume that there is a pair of piezoresistors whose <110> axis are aligned with the longitudinal axis. Each one of this is one of the resistors in the respective standard Wheatstone bridge circuits. When the beams twist, there will be a change in the resistance of the piezoresistor, which results in a change in voltage of the corresponding bridge circuit.

The stress was computed using hybrid elements and it was used in calculating the resulting piezoresistive coefficients and the change in resistance. It was done using the usual three-parameter piezoresistive tensor as well as the full-parameter tensor. The difference in the computed voltage is shown in Fig. 8. It can be seen

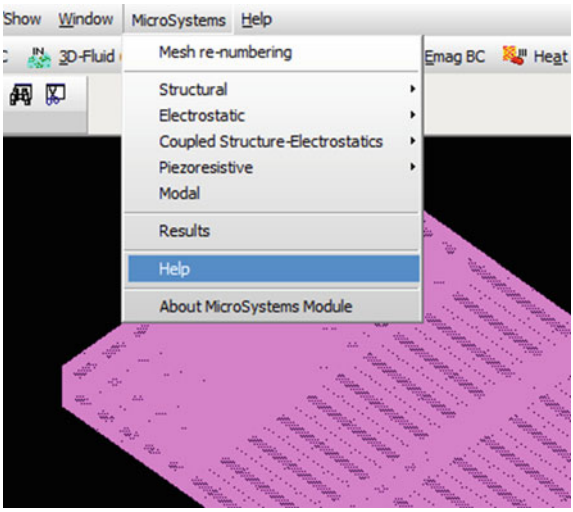

Fig. 9 Various capabilities of the microsystems simulation module

that there is as much as 33 % error between the two. Thus, in the software module we have developed, good accuracy is obtained irrespective of the alignment of the crystallographic axes of the piezoresistors with the main axes of the micromechanical structures. Hybrid elements are used in elastic analysis in this coupled code.

6 Integration of the Microsystem Module

As discussed in the preceding sections, by using the hybrid finite elements and other novel features, we have developed a simulation module for microsystems. It can be run as a stand-alone module with custom-developed graphical user interface or by interfacing it with a commercial finite element software. Here, for the purpose of illustration, we use NISA (www.cranessoftware.com). We use the DISPLAY IV module of NISA as a pre- and post-processor. That is, the model is created and material properties and boundary conditions are specified in the DISPLAY IV environment and the data is saved in the NISA environment. This file is read by our parser to write another data file that can be read and interpreted by our hybrid analysis codes. The results of the hybrid code is written to a file in the format of DISPLAY IV. The results are viewed in the GUI of NISA. This can be done, we emphasize, in any other commercial finite element software.

Figure 9 shows the current capabilities of the integrated microsystems simulation module, as can be seen in the pull-down menu item. A typical display of the result is shown in Fig. 10.

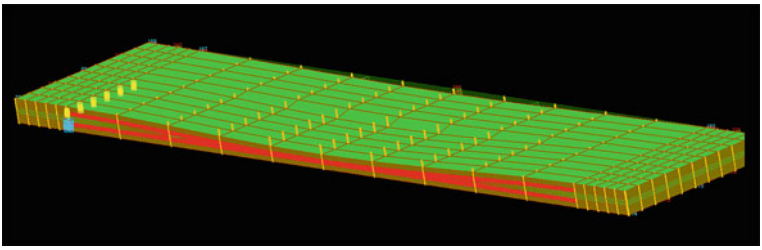

Fig. 10 Rendering of the deformed configuration of the pull-in of a fixed-fixed beam

7 Conclusions

In this chapter, we have addressed a critical need in the simulation of microsystems by allowing the users to work with a single type of finite element and obtain accurate results with a coarse mesh. It is accomplished by using hybrid finite elements where displacement and stress fields are both interpolated using suitable shape functions. It was shown that, the implementation will be seamless because the stress degrees of freedom are eliminated in terms of the nodal displacements. As a result, the new technique can be used in the same manner as the traditional displacement-based finite element simulation. The other important novel feature is the integrated solution strategy when more than one PDE is involved. Some other novel features are introduced in other capabilities of the simulation module. A representative simulation is presented for piezoresistive structures where it was shown that accuracy need not be compromised when the piezoresistor's crystallographic axes are not aligned with the coordinate system of the device. Some other capabilities of the microsystem module include modal, thermal, and electrothermal analyses.

Acknowledgments The authors gratefully acknowledge the financial support from the National Programme on Micro and Smart Systems (NPMASS), Government of India, under PARC 3.9 project entitled "Software Development and Scientific Computing for Micro and Nano Engineering". This work is a result of the synergistic efforts of numerous members of project staff and students in the Computational Nanoengineering (CoNe) group in the Indian Institute of Science, who worked on different aspects of implementing the hybrid and other codes and testing the initial versions of the simulation module. Help from Cranes Software International Limited, Bangalore, with the user-interface in NISA, is also gratefully acknowledged.

References

1. Senturia SD, Harris RM, Johnson BP et al (1992) A computer-aided design system for microelectromechanical systems (MEMCAD). J Micro Elecromech Syst 1(1):3–13
2. Senturia SD (2001) Microsystem design. Kluwer Academic Publishers, Boston
3. Bathe KJ (1996) Finite element procedures. Prentice Hall, Englewood Cliffs
4. Spilker RL, Singh SP (1982) Three-dimensional hybrid-stress isoparametric quadratic displacement elements. Int J Numer Meth Eng 18:445–465

5. Pian THH (1995) State-of-the-art development of hybrid/mixed finite element method. Finite Elem Anal Des 21:5–20
6. Pian THH, Chen DP, Kang D (1983) A new formulation of hybrid/mixed finite element. Comput Struct 16(1–4):81–87
7. Jog CS (2005) A 27-node hybrid brick and a 21-node hybrid wedge element for structural analysis. Finite Elem Anal Des 41:1209–1232
8. Jog CS (2010) Improved hybrid elements for structural analysis. J Mech Mater Struct 5(3):507–528
9. Sundaram MR, Ganesh G, Pavan K, Varun B, Jog CS, Ananthasuresh GK (2012) Static elastic simulation of microelectromechanical structures using hybrid finite elements. In: International conference on smart materials, structures and systems, 4–7 Jan, Bangalore
10. Jog CS, Kelkar PP (2006) Nonlinear analysis of structures using high-performance hybrid elements. Int J Numer Meth Eng 68:473–501
11. Rochus V, Rixen DJ, Golinval JC (2006) Monolithic modelling of electromechanical coupling in microstructures. Int J Numer Meth Eng 65:461–493
12. Yoon GH, Sigmund O (2008) A Monolithic approach for topology optimization of electrostatically actuated devices. Comput Meth Appl Mech Eng 197(45–48):4062–4075
13. Li G, Aluru NR (2002) A Lagrangian approach for electrostatic analysis of deformable conductors. J Microelecromech Syst 11:245–254
14. Alwan A, Ananthasuresh GK (2006) Coupled electrostatic-elastic analysis for topology optimization using material interpolation. J Phys Conf Ser 34:264–271
15. Patil KD, Jog, CS, and Ananthasuresh, GK (2014) Monolithic hybrid finite element strategy for coupled structure-electrostatic analysis of micromechanical structures. In: International conference on smart materials, structures and systems, 8–11 July, Bangalore
16. Balakrishnan S, Deshpande, K, and Ananthasuresh GK (2014) A note on modelling of directionality in piezoresistivity. J ISSS 3(1):1–8
17. Jog CS (2007) Continuum mechanics. Narosa Publishing House, New Delhi